

# Super-Resolution Power and Robustness of Compressive Sensing for Spectral Estimation With Application to Spaceborne Tomographic SAR

Xiao Xiang Zhu, *Student Member, IEEE*, and Richard Bamler, *Fellow, IEEE*

**Abstract**—We address the problem of resolving two closely spaced complex-valued points from  $N$  irregular Fourier domain samples. Although this is a generic super-resolution (SR) problem, our target application is SAR tomography (TomoSAR), where typically the number of acquisitions is  $N = 10\text{--}100$  and SNR = 0–10 dB. As the TomoSAR algorithm, we introduce “Scale-down by L1 norm Minimization, Model selection, and Estimation Reconstruction” (SL1MMER), which is a spectral estimation algorithm based on compressive sensing, model order selection, and final maximum likelihood parameter estimation. We investigate the limits of SL1MMER concerning the following questions. How accurately can the positions of two closely spaced scatterers be estimated? What is the closest distance of two scatterers such that they can be separated with a detection rate of 50% by assuming a uniformly distributed phase difference? How many acquisitions  $N$  are required for a robust estimation (i.e., for separating two scatterers spaced by one Rayleigh resolution unit with a probability of 90%)? For all of these questions, we provide numerical results, simulations, and analytical approximations. Although we take TomoSAR as the preferred application, the SL1MMER algorithm and our results on SR are generally applicable to sparse spectral estimation, including SR SAR focusing of point-like objects. Our results are approximately applicable to nonlinear least-squares estimation, and hence, although it is derived experimentally, they can be considered as a fundamental bound for SR of spectral estimators. We show that SR factors are in the range of 1.5–25 for the aforementioned parameter ranges of  $N$  and SNR.

**Index Terms**—Compressive sensing (CS), SAR tomography (TomoSAR), SL1MMER, spectral estimation, super-resolution (SR), synthetic aperture radar (SAR).

## I. INTRODUCTION

SAR TOMOGRAPHY (TomoSAR) uses stacks of repeat-pass SAR acquisitions to reconstruct the reflectivity of the scattering objects along elevation  $s$  by means of spectral analysis for every azimuth–range ( $x - r$ ) pixel [1]–[3]. With the German TerraSAR-X (TS-X) and the Italian COSMO-Skymed

Manuscript received June 16, 2010; revised January 10, 2011 and April 5, 2011; accepted June 12, 2011. Date of publication July 29, 2011; date of current version December 23, 2011. This work was supported by the International Graduate School of Science and Engineering, Technische Universität München, Munich.

The authors are with the Remote Sensing Technology Institute (IMF), German Aerospace Center (DLR), 82234 Oberpfaffenhofen, Germany, and also with Lehrstuhl für Methodik der Fernerkundung, Technische Universität München, 80333 Munich, Germany (e-mail: xiaoxiang.zhu@bv.tum.de; richard.bamler@dlr.de).

Color versions of one or more of the figures in this paper are available online at <http://ieeexplore.ieee.org>.

Digital Object Identifier 10.1109/TGRS.2011.2160183

satellites, SAR data with a very high spatial resolution (VHR) of up to 1 m are available. This resolution is particularly helpful when it comes to interferometric and tomographic imaging of buildings and urban infrastructure. The inherent spatial scales of these objects are in the meter range, e.g., typical height between floors of 3–3.5 m [4].

There are several challenges in fully exploiting the potential of this class of VHR data. First, compared to the airborne case, spaceborne data are collected over a longer time period. Temporal decorrelation thus reduces the signal-to-noise ratio (SNR) of coherent objects—for TS-X, the SNR caused by decorrelation is typically 0–10 dB [5]—calling for a larger number of acquisitions for accurate reconstruction. On the other hand, VHR data are expensive, and hence, the data stacks should be kept small. Second, nonlinear, e.g., thermal induced, deformations of different building parts must be expected, and this will introduce additional phase errors if not modeled. In this case, differential TomoSAR (D-TomoSAR) provides a solution [1], [3], [6]. Finally, in TomoSAR imaging, it would be favorable to have an isotropic tomographic spatial resolution element, i.e., an elevation resolution on the order of that in azimuth and range. This would require a huge elevation aperture of several kilometers. However, the tight orbit control of modern meter-resolution satellites leads to a tomographic elevation resolution  $\rho_s$  of about 10–50 times less than that in azimuth  $\rho_x$  or range  $\rho_r$  [3]. Those particular challenges call for robust super-resolution (SR) TomoSAR algorithms. In order to maintain the azimuth–range resolution for urban infrastructure imaging, these algorithms should not require averaging in azimuth and range.

The high anisotropy of the 3-D tomographic resolution element, together with the fact that thick volumetric scatterers tend to temporarily decorrelate in X-band, renders the signals *sparse* in the elevation direction, i.e., only a few point-like reflections along the elevation are expected per azimuth–range cell. For instance, TS-X in its high-resolution spotlight mode has a typical resolution of 1.1 m in azimuth, 0.6 m in range, and 30 m in elevation. Possible signal contributions in a single azimuth–range pixel could be point scatterers and rough surfaces. Their projections onto the elevation direction have a size of about 1/30 of the elevation resolution and, hence, can be treated as a few individual delta functions (typically 1–4) [10]. These kinds of signals are referred to as *sparse*. Considering the *sparsity* of the signals in the elevation direction, compressive sensing (CS) [7]–[9], as a favorable sparse reconstruction technique, has been recently introduced to radar [10]–[13] and TomoSAR reconstruction: the first CS TomoSAR simulations were presented in

[14], and the SR capability of CS for TomoSAR reconstruction and its robustness on elevation estimation against phase noise was proven in [15] using TS-X high-resolution spotlight data. However, the better performance of CS for elevation estimates over nonlinear least-squares (NLS) estimation is paid by the generation of occasional outliers, which leads to a reduced accuracy in complex-valued reflectivity estimation. Also, CS is known to slightly underestimate the amplitudes of scatterers. Therefore, we combine CS reconstruction with model selection and a final linear estimation of the complex amplitudes. Note that the CS TomoSAR algorithm has been recently introduced by the authors in [15], but it is presented here in more detail because the different algorithm steps are essential for the SR power. We name our CS-based TomoSAR spectral estimation algorithm as “Scale-down by L1 norm Minimization, Model selection, and Estimation Reconstruction” (*SLIMMER*, pronounced as “slimmer”). It combines the advantages of CS with the amplitude and phase accuracy of linear estimators.

In this paper, we investigate the limits of the technique by addressing the following three questions.

- 1) How accurately can the positions of two closely spaced scatterers be estimated? We give both numerical results and analytical approximation.
- 2) What is the closest distance of two scatterers such that they can be separated with a detection rate of 50% at given  $N \cdot \text{SNR}$  and amplitude ratio with a uniformly distributed phase difference? We find the SR factors by extensive simulations and provide an easy-to-use polynomial approximation.
- 3) How many acquisitions  $N$  are required for a *robust* estimation (i.e., for separating two scatterers spaced by one Rayleigh resolution unit with a probability of 90%)?

Although we take TomoSAR as the preferred application, the SLIMMER algorithm and our results on SR are generally applicable to sparse spectral estimation, including SAR focusing of point-like objects. We will also show that our proposed SLIMMER algorithm provides an aesthetic approximation of the NP-hard  $L_0$  norm regularization, which is equivalent to an NLS plus model selection (see Section III), and hence, our results are approximately applicable to NLS estimation. They are asymptotically optimal, with an estimation accuracy approaching the Cramér–Rao lower bound (CRLB). As a consequence, although it is derived experimentally, our results can be considered as the fundamental bounds for the SR capability of spectral estimators.

This paper is organized as follows. Section II gives a brief introduction to TomoSAR imaging model. Section III provides an overview on inversion methods and regularizers. The basic idea of the SLIMMER algorithm is presented in Section IV. Section V derives the CRLB of elevation estimation for two interfering scatterers with a uniformly distributed phase difference and further analyzes the elevation estimation accuracy of the algorithm. Sections VI and VII investigate the SR power and robustness of the proposed algorithm for TomoSAR, and the conclusion is drawn in the last section. For all of our simulations, we assume a range of  $N = 10\text{--}100$  and  $\text{SNR} = 0\text{--}10 \text{ dB}$ , i.e.,  $N \cdot \text{SNR} = 10\text{--}30 \text{ dB}$ .

## II. TOMOGRAPHIC SAR IMAGING MODEL

TomoSAR inversion starts from a stack of  $N$  complex SAR data sets of the same area taken at different times and slightly different orbit positions (the elevation aperture). Let the elevation aperture positions, i.e., the perpendicular baselines with respect to a master track, be  $b_n$ . After some trivial phase corrections, the focused complex value  $g_n$  of an azimuth–range pixel  $(x_0, r_0)$  of the  $n$ th acquisition is [2], [16]

$$g_n = \int_{\Delta s} \gamma(s) \exp(-j2\pi\xi_n s) ds \quad (1)$$

where  $\gamma(s)$  represents the reflectivity function along elevation  $s$  and  $\Delta s$  describes the range of possible elevations.  $\xi_n = -2b_n/(\lambda r_0)$  is the spatial (elevation) frequency depending on the (more or less random) elevation aperture position  $b_n$ , where  $\lambda$  stands for the wavelength. Equation (1) is a randomly sampled Fourier transform of  $\gamma(s)$ . From this, we expect an inherent Rayleigh resolution in elevation of  $\rho_s = \lambda r/(2\Delta b)$ , where  $\Delta b$  is the elevation aperture size. The system model (1) can be approximated by discretizing the object along  $s$ , and in the presence of the noise  $\varepsilon$ , it can be written as (ignoring an inconsequential constant)

$$\mathbf{g} = \mathbf{R}\boldsymbol{\gamma} + \boldsymbol{\varepsilon} \quad (2)$$

where  $\mathbf{g}$  is the measurement vector of length  $N$ ;  $\mathbf{R}$ , with  $R_{n \times l} = \exp(-j2\pi\xi_n s_l)$ , is an  $N \times L$  mapping (Fourier transform) matrix; and  $\boldsymbol{\gamma}$  is  $\gamma(s)$  uniformly sampled in elevation at  $s_l$  ( $l = 1, \dots, L$ ).

Taking the motion terms into account, the system model (1) can be extended to D-TomoSAR [1]. Its 2-D inversion provides retrieval of the elevation and deformation information even of multiple scatterers inside an azimuth–range resolution cell, thus obtaining a 4-D map of scatterers. Extensions to multimodal motion models are possible, but they require an even higher dimensional spectral estimation inversion [6]. For the sake of simplicity, we restrict ourselves to the 1-D spectral estimation case here.

## III. INVERSION METHODS AND REGULARIZERS

Since  $L \gg N$ , the system model (2) is severely underdetermined. Hence, there are infinitely many solutions. Depending on the type of prior (i.e., regularizer), different solutions can be obtained.

### A. $L_2$ Norm Regularization

The conventional TomoSAR algorithms are based on the  $L_2$  norm regularization, also referred to as Tikhonov regularization

$$\hat{\boldsymbol{\gamma}} = \arg \min_{\boldsymbol{\gamma}} \left\{ \|\mathbf{g} - \mathbf{R}\boldsymbol{\gamma}\|_2^2 + \|\boldsymbol{\Gamma}\boldsymbol{\gamma}\|_2^2 \right\} \quad (3)$$

for some suitably chosen Tikhonov matrix  $\boldsymbol{\Gamma}$ . For Gaussian stationary white measurement noise, i.e.,  $\mathbf{C}_{\boldsymbol{\varepsilon}\boldsymbol{\varepsilon}} = \sigma_\varepsilon^2 \mathbf{I}$ , and Gaussian prior with covariance matrix  $\boldsymbol{\Gamma}^{-(1/2)}$ , this is the

standard MAP estimator. The special case of white prior, i.e.,  $\Gamma = \mathbf{I}$ , renders (3) to

$$\hat{\gamma} = \arg \min_{\gamma} \left\{ \|\mathbf{g} - \mathbf{R}\gamma\|_2^2 + \sigma_\varepsilon^2 \|\gamma\|_2^2 \right\}. \quad (4)$$

This estimator was named ‘‘SVD Wiener’’ in [3]. Another choice of  $\Gamma$  leads to the well-known truncated SVD estimator [16].

As a nonparametric estimator, (4) is computationally efficient and does not require any assumption about the number of scatterers. However, it suffers from the sidelobe problem and does not provide super resolving capability.

### B. $L_0$ Norm Regularization

As described in the introduction and as outlined in detail in [15],  $\gamma$  is *sparse* in the object (elevation) domain for VHR spaceborne X-band TomoSAR with typically 1–4 point-like contributions of unknown positions, amplitudes, and phases, i.e.,  $\gamma$  is assumed to contain only  $K = 1–4$  nonzero elements.

This *sparsity* property of  $\gamma$  suggests the use of the CS approach. It says that, if the mapping matrix fulfills certain requirements, i.e., the *restricted isometry property (RIP)* and the *incoherence* property [9], with the number of measurements depending on the sparsity  $K$  instead of the length of the signal  $L$ ,  $\gamma$  can be very well approximated by the solution with the least number of scatterers (nonzero elements of  $\gamma$ ), i.e., the minimal  $L_0$  norm, which satisfies the measurements with noise

$$\min_{\gamma} \|\gamma\|_0 \quad \text{s.t.} \quad \mathbf{g} = \mathbf{R}\gamma. \quad (5)$$

In the presence of measurement noise, the estimator can be written as

$$\hat{\gamma} = \arg \min_{\gamma} \left\{ \|\mathbf{g} - \mathbf{R}\gamma\|_2^2 + \lambda_{MS} \|\gamma\|_0 \right\}. \quad (6)$$

This is an NLS parametric estimator, i.e., a maximum likelihood estimator (MLE) under Gaussian noise, plus a model complexity penalty term. By choosing  $\lambda_{MS} = 3\sigma_\varepsilon^2 \ln N$ , the penalty term is equivalent to the Bayesian information criterion (BIC) model selection scheme, which will be addressed in the next section.

Due to the sparse nature of the signal in elevation direction, the minimization of the  $L_0$  norm should be the correct way to find the exact solution, even with two scatterers closer than a resolution cell. However, it is an N-P hard problem. Therefore, except if we limit ourselves to the cases with only one or two scatterers and in a *single* dimension—elevation—(i.e., no extension to D-TomoSAR), we need a more efficient algorithm.

### C. $L_1$ Norm Regularization (CS)

The CS theory tells us that, if the mapping matrix  $\mathbf{R}$  fulfills the RIP and incoherence properties and  $N = O(K \log(L/K))$ , the *convex*  $L_1$  norm minimization gives the same solution as the N-P hard  $L_0$  norm minimization. In case if there is no prior knowledge about  $K$  and in the presence of measurement

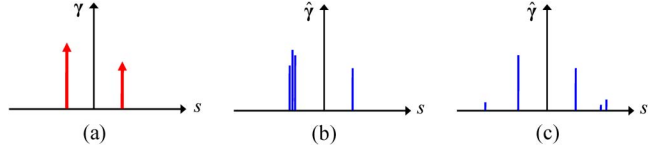


Fig. 1. Violation of RIP and incoherence properties may cause artifacts in the reconstruction. (a) True reflectivity profile. (b) Reconstruction of a scatterer by several adjacent lines instead of a single peak. (c) Reconstruction with noise-like outliers.

noise, it can be approximated by the following  $L_1-L_2$  norm minimization [15]:

$$\hat{\gamma} = \arg \min_{\gamma} \left\{ \|\mathbf{g} - \mathbf{R}\gamma\|_2^2 + \lambda_K \|\gamma\|_1 \right\} \quad (7)$$

where  $\lambda_K$  is the Lagrange multiplier as a function of  $N$  and  $\varepsilon$  [22], [27]. The CS estimator of (7) has approximately the same SR capability as (6), but it is more robust to phase noise, needs less computational effort, and does not require model selection to provide the prior knowledge about the number of scatterers  $K$ .

### D. Drawbacks of the CS Estimator

The simple CS estimator (7) has two drawbacks, which will be discussed in the following. Both are corrected in the proposed SL1MMER algorithm.

*RIP and Incoherence:* RIP guarantees the sufficiently sparse reconstruction in the presence of noise. It essentially says that all submatrices of  $\mathbf{R}$  composed of  $K$  columns should be nearly orthogonal, and hence, they preserve the energy of all vectors having only nonzero elements at the same  $K$  positions as  $\gamma$ . *Incoherence* means that the mapping operator  $\mathbf{R}$  will spread out information of sparse (highly localized) signals in the entire measurement space (like a Fourier transform does), thus making them insensitive to random undersampling.

However, for many applications, like TomoSAR, RIP and incoherence are violated for several reasons. First, the mapping matrix  $\mathbf{R}$  is predetermined by the measurement system (the elevation aperture sampling pattern) and may not be optimum. Second, the profile  $\gamma(s)$  to be reconstructed is often sampled much more densely than the elevation resolution unit in order to allow good resolution and scatterer positioning accuracy. This small sampling distance renders  $\mathbf{R}$  overcomplete, reduces RIP [15], and increases coherence. As a consequence, the CS estimator (7) will not always give the solution with the correct number of scatterer  $K$ . It may produce spurious artifacts. There are two classes of artifacts shown schematically in Fig. 1. If the sampling raster is very dense, single scatterers may be broadened to a few adjacent lines [Fig. 1(b)]; however, they are well within a Rayleigh resolution unit. With a certain probability, small spurious impulses may show up [Fig. 1(c)].

*Amplitude Bias:* Although the CS estimator (7) is radiometrically much more reliable than MUSIC, CAPON, AR, etc., it will slightly, yet systematically, underestimate the amplitudes of the scatterers because the  $L_1$  prior favors smaller amplitudes.

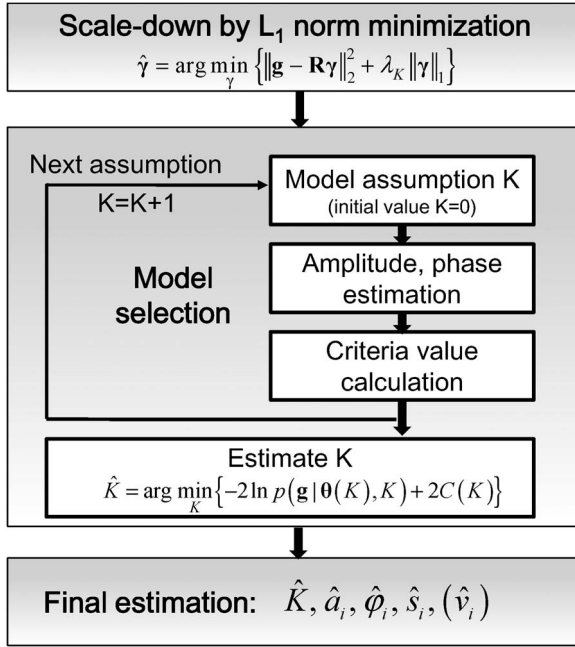


Fig. 2. Flow chart of the SL1MMER algorithm. Note that, in the final estimation step, a motion parameter  $\hat{v}$  shows up since the SL1MMER algorithm has originally been implemented for D-TomoSAR. However, to keep the mathematics of this paper simpler, we neglect motion for our study.

#### IV. SL1MMER ALGORITHM

The artifacts described in the last section are not critical when the aim is only to reconstruct a reasonable reflectivity profile. However, high-quality sparse tomographic SAR inversion requires the estimation of the number of scatterers, as well as the amplitude, phase, and elevation of each scatterer. Hence, special care must be taken to those nuisance artifacts. As will be shown, the SL1MMER algorithm improves the CS algorithm and estimates these parameters in a very accurate and robust way. It consists of three main steps: 1) dimensionality scale-down by  $L_1$  norm minimization; 2) model selection; and 3) parameter estimation (see Fig. 2).

##### A. Scale-Down by $L_1$ Norm Minimization

For dimensionality reduction, the  $L_1 - L_2$  norm minimization from (7) has been implemented at the first stage, which gives a robust estimate of the plausible positions of the scatterers, among which there might be a few outliers contributed by noise. By only selecting its columns corresponding to the nonzero elements of  $\hat{\gamma}$ , the mapping matrix  $\mathbf{R}$  is scaled down significantly. It renders the severely underdetermined system model finally overdetermined.

##### B. Model Selection

The  $L_1 - L_2$  norm minimization step shrinks  $\mathbf{R}$  dramatically and gives a first sparse estimate of  $\gamma$ . This estimate, though, may still contain the aforementioned outliers (Fig. 1), and hence, the sparsity  $K$  (i.e., the number of the scatterers) is often overestimated. Model selection is used to clean the  $\gamma$  estimate of spurious nonsignificant scatterers and to finally obtain the

most likely number  $\hat{K}$  of scatterers inside an azimuth–range cell [17]. It provides a tradeoff between the model complexity and the model fit.

The model complexity can be described by the number of parameters  $k$ . In our case,  $k = 3K$  since each scatterer is characterized by three parameters (amplitude, phase, and elevation). Let  $\theta(K)$  further be the vector of the unknown amplitudes, phases, and elevations for all of the  $K$  scatterers. The goodness of model fit can be described by the likelihood  $p(\mathbf{g}|\hat{\theta}(K), K)$ . A more complex model always fits the observations better, and hence, for the purpose of selecting the true model, the complexity of the model must be penalized to avoid overfitting of the data. This reveals the main concept of penalized likelihood criteria. The general form of the penalized likelihood criteria is [18]

$$\hat{K} = \arg \min_K \left\{ -2 \ln p(\mathbf{g}|\hat{\theta}(K), K) + 2C(K) \right\} \quad (8)$$

where  $C(K)$  is the complexity penalty. Note that, for stationary white Gaussian measurement noise,  $-2 \ln p(\mathbf{g}|\hat{\theta}(K), K) = \sigma_e^2 \|\mathbf{g} - \mathbf{R}\hat{\gamma}\|_2^2$ . Many types of penalty terms are proposed in the literature, e.g., the BIC [19], the Akaike information criterion [20], and the minimum description length [21]. As shown in Fig. 2, for each model assumption  $K = 0, \dots, 4$ , the elevations are given by the previous scale-down step, and thus, the amplitudes and phases can be easily obtained by linear least-squares estimation. The preferred number of scatterers  $\hat{K}$  inside an azimuth–range cell is finally the one with the lowest penalized likelihood criterion value according to (8). The implementation details of different model selection schemes for VHR TomoSAR are addressed in [3]. We use the BIC penalized likelihood criterion with a penalty term  $C(K) = 0.5k \ln N = 1.5K \ln N$  throughout this paper with the same parameter setting, i.e., the subsequent comparison between different algorithms is independent from the model selection schemes.

##### C. Parameter Estimation

As a last refinement, a much slimmer mapping matrix  $\mathbf{R}(\hat{\mathbf{s}})$ , i.e., the  $N \times \hat{K}$  matrix with  $\mathbf{R}_{n,k}(\hat{\mathbf{s}}) = \exp(-j2\pi\xi_n \hat{s}_k)$ , is built up, and the final complex-valued reflectivity  $\hat{\gamma}(\hat{\mathbf{s}})$  for the  $\hat{K}$  scatterer is obtained by solving the following overdetermined linear system equation:

$$\mathbf{g} = \mathbf{R}(\hat{\mathbf{s}})\hat{\gamma}(\hat{\mathbf{s}}) + \mathbf{e} \quad (9)$$

where  $\mathbf{e}$  combines the measurement noise and the model error, i.e., the deviation from sparsity or unmodeled motion-induced phase terms (in the D-TomoSAR case). The sparse reflectivity profile  $\hat{\gamma}(\hat{\mathbf{s}})$  is finally found by

$$\hat{\gamma}(\hat{\mathbf{s}}) = (\mathbf{R}^H(\hat{\mathbf{s}})\mathbf{R}(\hat{\mathbf{s}}))^{-1} \mathbf{R}^H(\hat{\mathbf{s}})\mathbf{g}. \quad (10)$$

By introducing model selection (8) and refinement of the parameter estimation (10), SL1MMER improves the result of CS by means of removing possible outliers and providing more accurate amplitude and phase estimates.

## V. ESTIMATION ACCURACY

### A. CRLB for Two Scatterers

Assuming two scatterers at elevation positions  $s_1$  and  $s_2$  with amplitudes  $a_1$  and  $a_2$  and phases  $\varphi_1$  and  $\varphi_2$ , the (noise-free) measurements according to the system model (2) are

$$\bar{\mathbf{g}}(\boldsymbol{\theta}) = [\bar{g}_1(\boldsymbol{\theta}), \bar{g}_2(\boldsymbol{\theta}), \dots, \bar{g}_N(\boldsymbol{\theta})]^T$$

where

$$\bar{g}_n(\boldsymbol{\theta}) = \sum_{q=1}^2 a_q \exp(j(2\pi\xi_n s_q + \varphi_q)) \quad (11)$$

and the parameter vector

$$\boldsymbol{\theta} = [\theta_1, \theta_2, \dots, \theta_6]^T = [a_1, \varphi_1, s_1, a_2, \varphi_2, s_2]^T. \quad (12)$$

Then, the data vector according to (2), including the zero-mean circular Gaussian noise, is

$$\mathbf{g} = [g_1, \dots, g_N]^T \quad (13)$$

with mean

$$\bar{\mathbf{g}}(\boldsymbol{\theta}) = E\{\mathbf{g}\}$$

$$= \begin{bmatrix} \exp(j2\pi\xi_1 s_1) & \exp(j2\pi\xi_1 s_2) \\ \vdots & \vdots \\ \exp(j2\pi\xi_N s_1) & \exp(j2\pi\xi_N s_2) \end{bmatrix} \begin{bmatrix} a_1 \exp(j\varphi_1) \\ a_2 \exp(j\varphi_2) \end{bmatrix} \quad (14)$$

and covariance matrix

$$\mathbf{C}_{\varepsilon\varepsilon} = \sigma_\varepsilon^2 \mathbf{I}. \quad (15)$$

The likelihood function is given by

$$p(\mathbf{g}|\boldsymbol{\theta}) = \frac{1}{(2\pi)^N |\mathbf{C}_{\varepsilon\varepsilon}|} \exp\left(-(\mathbf{g} - \bar{\mathbf{g}}(\boldsymbol{\theta}))^H \mathbf{C}_{\varepsilon\varepsilon}^{-1} (\mathbf{g} - \bar{\mathbf{g}}(\boldsymbol{\theta}))\right). \quad (16)$$

From the *Fisher information matrix*

$$\mathbf{J} = -E\left\{\frac{\partial^2 \ln p(\mathbf{g}|\boldsymbol{\theta})}{\partial \boldsymbol{\theta} \partial \boldsymbol{\theta}^T}\right\} \quad (17)$$

we derive the CRLB  $\mathbf{P}_{\text{CR}} = \mathbf{J}^{-1}$ . For our idealized data statistics (12)–(14)[22]

$$J_{ij} = 2\text{Re}[\bar{\mathbf{g}}_i^H \mathbf{C}_{\varepsilon\varepsilon}^{-1} \bar{\mathbf{g}}_j] \quad (18)$$

where  $\bar{\mathbf{g}}'_i$  denotes the derivative of  $\bar{\mathbf{g}}$  with respect to the  $i$ th element of  $\boldsymbol{\theta}$

$$\begin{aligned} \bar{\mathbf{g}}'_n &= \left[ \frac{\partial \bar{g}_n}{\partial \theta_1}, \dots, \frac{\partial \bar{g}_n}{\partial \theta_6} \right]^T \\ &= [\exp(j(2\pi\xi_n s_1 + \varphi_1)) [1 \quad ja_1 \quad j2\pi\xi_n a_1], \\ &\quad \exp(j(2\pi\xi_n s_2 + \varphi_2)) [1 \quad ja_2 \quad j2\pi\xi_n a_2]]^T. \end{aligned} \quad (19)$$

The Fisher information matrix for our two-scatterer case can be written as

$$\mathbf{J} = \begin{bmatrix} \mathbf{J}_{11} & \mathbf{J}_{12} \\ \mathbf{J}_{12}^T & \mathbf{J}_{22} \end{bmatrix} \quad (20)$$

where  $\mathbf{J}_{11}$  and  $\mathbf{J}_{22}$  describe the Fisher information matrices of the individual isolated scatterers (i.e., in the absence of the other one)

$$\mathbf{J}_{qq} = \frac{2}{\sigma_\varepsilon^2} \cdot \begin{bmatrix} N & 0 & 0 \\ 0 & a_q^2 N & 2\pi a_q^2 \sum_N \xi_n \\ 0 & 2\pi a_q^2 \sum_N \xi_n & 4\pi^2 a_q^2 \sum_N \xi_n^2 \end{bmatrix}, \quad q = 1 \text{ or } 2.$$

$\mathbf{J}_{12}$  contributes to the interference between them. Let us define  $\Delta := 2\pi\xi_n \delta_s + \Delta\varphi$ , where  $\delta_s = s_2 - s_1$  and  $\Delta\varphi = \varphi_2 - \varphi_1$  are, respectively, the distance and phase difference between the two scatterers, and  $\mathbf{J}_{12}$  is given by the equation shown at the bottom of the page.

Note that the elevation aperture positions  $\xi_n$  show up in the Fisher information matrix only in the form of moments of their distribution. Hence, for sufficiently large  $N$ , there will be no difference between a regularly sampled aperture and a uniformly randomly sampled one.

Since the analytical inversion of  $\mathbf{J}$ —although possible—leads to a complicated and lengthy expression, we retrieve the relevant elements of the CRLB matrix by solving the inversion numerically. From the CRLB matrix  $\mathbf{P}_{\text{CR}} = \mathbf{J}^{-1}$ , the elements  $P_{\text{CR},3,3} = \sigma_{s_1}^2$  and  $P_{\text{CR},6,6} = \sigma_{s_2}^2$  are most of interest, i.e., the CRLBs of the location estimation errors for the two scatterers.

For the sequel, we split the elevation estimation error into two contributions

$$\sigma_{s_q} = c_0 \cdot \sigma_{s_q,0} \quad (21)$$

where

$$\sigma_{s_q,0} = \frac{\lambda r_0}{4\pi\sqrt{2} \cdot \sqrt{N \cdot SNR_q} \cdot \sigma_b} \quad (22)$$

$$\mathbf{J}_{12} = \frac{2}{\sigma_\varepsilon^2} \cdot \begin{bmatrix} \sum_N \cos \Delta & -a_2 \sum_N \sin \Delta & -2\pi a_2 \sum_N \xi_n \sin \Delta \\ a_1 \sum_N \sin \Delta & a_1 a_2 \sum_N \cos \Delta & 2\pi a_1 a_2 \sum_N \xi_n \cos \Delta \\ 2\pi a_1 \sum_N \xi_n \sin \Delta & 2\pi a_1 a_2 \sum_N \xi_n \cos \Delta & 4\pi^2 a_1 a_2 \sum_N \xi_n^2 \cos \Delta \end{bmatrix}$$

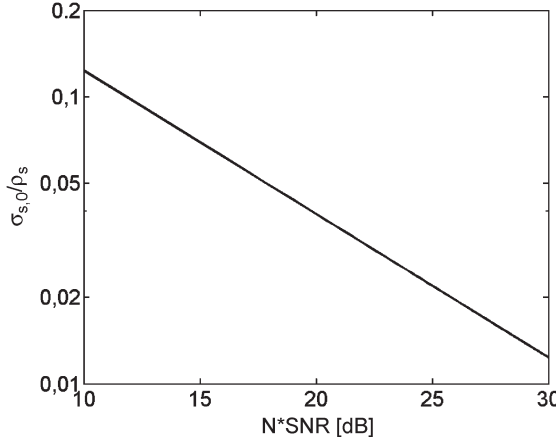


Fig. 3. CRLB  $\sigma_{s,0}$  of the elevation estimation accuracy of a single scatterer, normalized to the elevation resolution, as a function of  $N \cdot \text{SNR}$ .

is the CRLB of the elevation estimates of the  $q$ th scatterer in the absence of the other one.  $\sigma_b$  is the standard deviation of the elevation aperture sample positions  $b_n$ . For uniformly distributed baselines (randomly or equidistantly spaced),  $\sigma_b = \rho_s/\sqrt{12}$  and  $\sigma_{s_q,0}$  can be related to the elevation resolution  $\rho_s$  by [4]

$$\sigma_{s_q,0} = \frac{\sqrt{3/2}}{\pi} \frac{\rho_s}{\sqrt{N \cdot \text{SNR}_q}} \approx \frac{0.39}{\sqrt{N \cdot \text{SNR}_q}} \rho_s \quad (23)$$

and  $c_0$  is the essential interference correction factor for closely spaced scatterers. It is almost independent from  $N$  and SNR. As a reference, in Fig. 3, we plot  $\sigma_{s_q,0}$ , normalized to the Rayleigh resolution unit  $\rho_s$ , as a function of  $N \cdot \text{SNR}_q$  to explore its impact on estimation accuracy, where  $\sigma_{s_q,0}$  follows exactly a  $-0.5$  power law. In the parameter range that we consider here, i.e.,  $N = 10\text{--}100$  and  $\text{SNR} = 0\text{--}10$  dB, the elevation estimation accuracy of a single scatterer is on the order of roughly  $1/100\text{--}1/10$  of the resolution unit.

For the subsequent discussion, we only consider the impact of the normalized CRLB  $c_0 = \sigma_s/\sigma_{s,0}$ .

If one wants to avoid the numerical inversion of the Fisher information matrix, an experimental approximation of  $c_0$  with a relative error within 2% was proposed in [23].

Modified after [23], (24) can be derived, shown at the bottom of the page, where  $\alpha = \delta_s/\rho_s$  is the distance between the two scatterers, normalized to the Rayleigh resolution unit, and  $\delta_b$  is the center position of the elevation aperture  $\Delta b$ . Without loss of generality, the elevation aperture is set to be  $[-\Delta b, \Delta b]/2$ , i.e.,  $\delta_b = 0$ . Equation (24) says that, for a fixed elevation aperture (i.e.,  $\Delta b$  and  $\delta_b$ ),  $\sigma_{s_q}$  depends asymptotically on the normalized distance  $\alpha$ ,  $N \cdot \text{SNR}_q$  (for sufficiently large  $N$ ), and phase difference  $\Delta\varphi$ . Figs. 4–6 show the normalized CRLB standard deviation  $c_0 = \sigma_s/\sigma_{s,0}$  of the elevation estimation error obtained by the numerical inversion of (20).

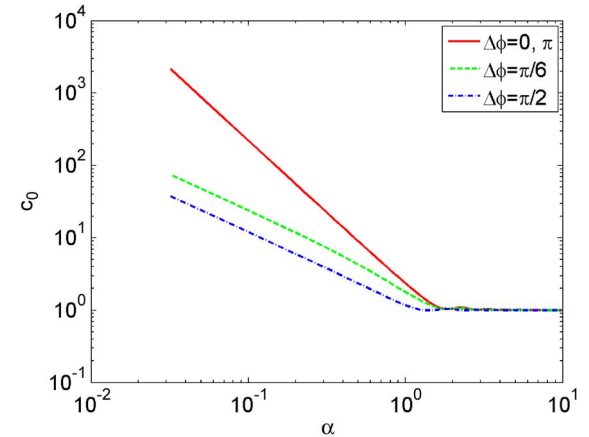


Fig. 4. Normalized CRLB  $c_0 = \sigma_s/\sigma_{s,0}$  of the elevation estimation accuracy of two close scatterers, normalized to the one of a single scatterer, as a function of normalized distance  $\alpha$  between two scatterers of the same amplitude and with different values of the phase difference  $\Delta\varphi$ .

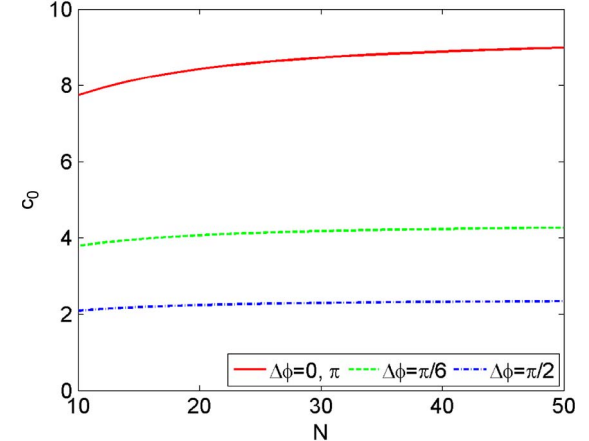


Fig. 5. Normalized CRLB  $c_0$  as function of  $N$  with different values of  $\Delta\varphi$  ( $\alpha = 0.5$  and  $\text{SNR} = 6$  dB).

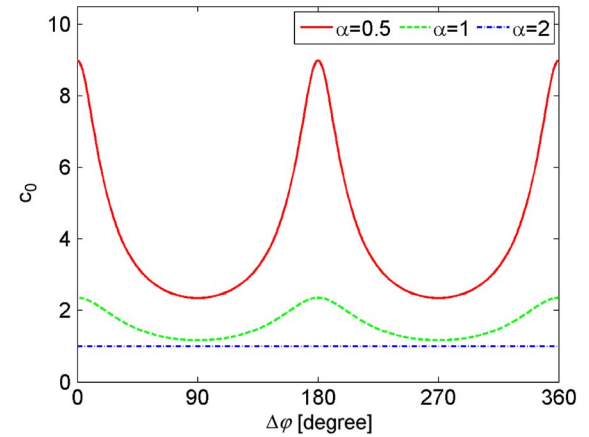


Fig. 6. Normalized CRLB  $c_0$  as a function of the phase difference  $\Delta\varphi$  between two scatterers with different values of  $\alpha$ .

$$c_0 = \sqrt{\max \left\{ \frac{40\alpha^{-2}(1 - \alpha/3)}{9 - 6(3 - 2\alpha) \cos(2\Delta\varphi + 2\pi\alpha(\frac{2\delta_b}{\Delta b} - \frac{1}{N})) + (3 - 2\alpha)^2}, 1 \right\}} \quad (24)$$

Fig. 4 shows  $c_0$  as a function of  $\alpha$ , with different values of  $\Delta\varphi$ . If the two scatterers are separated by much more than one Rayleigh resolution unit, i.e.,  $\alpha \gg 1$ , their elevation estimation accuracy is the one of individual scatterers, i.e.,  $c_0$  approaches one. The closer they move, the more they interfere, and the larger their elevation estimation error becomes, i.e.,  $c_0 > 1$ . The worst case is  $\Delta\varphi = 0$  or  $\pi$ , where  $c_0$  follows approximately a  $-2$  power law. The least interference between the scatterers occurs at  $\Delta\varphi = \pi/2$ , with a  $c_0$  power law of approximately  $-1$ . For our SR study, the case of  $\alpha < 1$  is of interest.

Besides the  $N \cdot \text{SNR}_q$  term in  $\sigma_{s,0}$ ,  $1/N$  appears in the argument of the cosine of (24), i.e., for small  $N$ ,  $c_0$  has a nonnegligible additional dependence on  $N$ . Fig. 5 shows  $c_0$  as a function of  $N$  under different  $\Delta\varphi$ , with  $\alpha = 0.5$  and  $\text{SNR} = 6$  dB. Except for the most unfavorable phase differences  $\Delta\varphi = 0$  and  $\pi$ , the effect of  $N$  is negligible once  $N > 15$ . Hereafter, we will neglect this effect, and all experiments are based on sufficiently large  $N$ . The situation of small  $N$  will be discussed in Section VII.

The phase difference  $\Delta\varphi$  appears multiplied by two in the argument of the cosine of (24). Therefore, in Figs. 4 and 5, the cases  $\Delta\varphi = 0$  and  $\Delta\varphi = \pi$  are identical. Fig. 6 analyzes  $c_0$  as a function of  $\Delta\varphi$ , with different values of  $\alpha$ . Intuitively, this phase behavior can be understood as follows: two scatterers with orthogonal complex-valued reflectivities (i.e.,  $\Delta\varphi = \pi/2$ ) use the two “channels” of complex measurements most efficiently, and hence, they can be better localized and identified than those with nonorthogonal ones. In particular,  $\Delta\varphi = 0$  and  $\Delta\varphi = \pi$  are the worst cases, i.e., the reflectivities of the two scatterers are collinear in the complex plane. Not surprisingly, the closer the two scatterers are, i.e., the smaller  $\alpha$ , the more pronounced is the dependence on their phase difference. Since, for our SR study, the case of small  $\alpha$  is particularly of interest, the impact of  $\Delta\varphi$  must be considered. For TomoSAR, the phase difference  $\Delta\varphi$  is a random variable because it depends on the unknown geometric configuration [24]. Hence, we calculate the CRLB for the elevation estimation error by integrating the variances over  $\Delta\varphi$ . The resulting dependence can be approximated by the following analytical expression:

$$c_0^2 = \frac{\sigma_s^2}{\sigma_{s,0}^2} \approx \max \left\{ 2.57(\alpha^{-1.5} - 0.11)^2 + 0.62, 1 \right\}. \quad (25)$$

It fits the CRLB in this range of  $\alpha$  better than the approximation derived in [23] ( $c_0^2 = \max \{(15/\pi^2)^{2.5} \alpha^{-3}, 1\}$ ). The square root of the normalized CRLB variance integrated over  $\Delta\varphi$  as a function of  $\alpha$  is shown in Fig. 7 together with our approximation. The dependence on  $\alpha^{-1.5}$  can be clearly observed.

## B. Elevation Estimation Accuracy

The normalized standard deviation of the elevation estimates for two interfering scatterers using NLS and SL1MMER as a function of  $\alpha$  is shown in Fig. 7. These have been obtained by simulations with randomly distributed phase differences. The elevation estimation accuracy of SL1MMER approaches the CRLB and is comparable to NLS. It is worth mentioning that, for the leftmost experiment point, i.e., for  $\alpha = 0.47$ , the

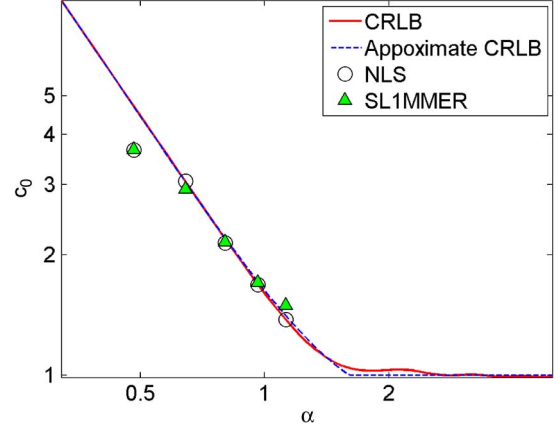


Fig. 7. Theory versus approximation versus experiments. Normalized CRLB  $c_0$  integrated over  $\Delta\varphi$  as a function of  $\alpha$ .

NLS and SL1MMER pretend to have a better accuracy than the CRLB. This is caused by the fact that we always assume that the two closely spaced scatterers never exchange their positions, which is not valid while moving the two scatterers closer such that the standard deviation increases and reaches the order of the distance between them.

## VI. SR POWER

Nonlinear and parametric spectral estimation methods yield reconstructions with much sharper point responses than traditional nonparametric linear algorithms. One might be tempted to infer a very high resolution power from this narrow point response width. However, the needle-like responses tell us neither the location accuracy of the individual points nor the ability of the algorithm to resolve two close scatterers. In this paper, the (elevation) resolution is defined by the *minimum distance*  $\rho_{PD}$  between two  $\delta$  functions (scatterers) that are separable at a given SNR with a certain number of measurements  $N$  and at a prespecified probability of detection  $P_D$ . As in the preceding sections, we normalize resolution to the Rayleigh resolution unit  $\rho_s$ . The *SR factor*  $\kappa_{PD}$  is defined by

$$\kappa_{PD} = \frac{\rho_s}{\rho_{PD}}. \quad (26)$$

It depends on the required detection rate  $P_D$  and is larger than unity for SR. In this section, the SR power for different  $N$ s, SNRs, amplitude ratios, and phase differences of the two scatterers will be investigated.

### A. Detection Rate Study

The problem of resolution can be regarded as a hypothesis test:

$H_0$ : null or only one scatterer inside the given azimuth-range cell;

$H_1$ : two scatterers inside the given azimuth-range cell.

In [25], the detection probability of two real-valued sinusoids with closely spaced frequencies is studied, and a sophisticated *detector* is proposed. Our goal, however, is to derive the SR

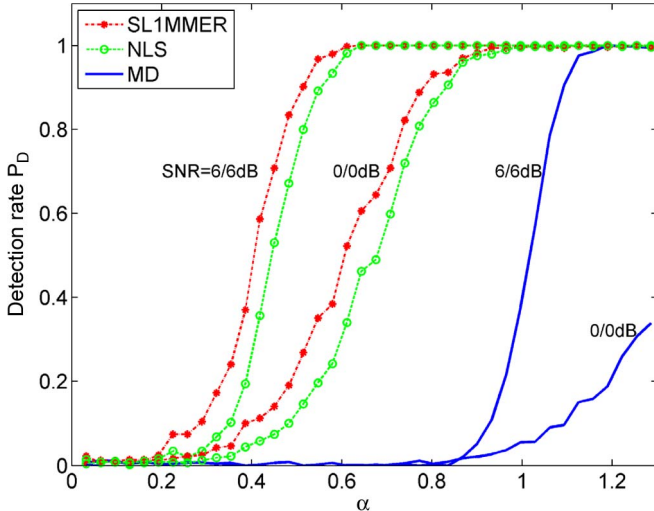


Fig. 8. Detection rate as a function of  $\alpha$  using SL1MMER (dashed star), NLS (dashed circle), and MD (solid), with  $\text{SNR} = 0/0$  and  $6/6$  dB,  $N = 25$ , and  $\Delta\varphi = 0$  (worst case).

power of an *estimator* that also provides location, amplitude, and phase of each scatterer.

Since it is very complicated to find a theory supporting all possible situations, we approach the problem experimentally. We start with an example of detecting two scatterers with the same amplitudes and phases by using  $N = 25$  regularly sampled acquisitions. Fig. 8 shows the detection rate  $P_D$  as a function of normalized distance  $\alpha$  at different SNR levels using SL1MMER, NLS, and linear reconstruction, followed by the detection of the maxima (MD) [3]. The phase difference in this simulation is  $\Delta\varphi = 0$ , i.e., the worst case. The SNR of each scatterer for the two sets of curves is 0 and 6 dB, respectively. This plot gives us several perspectives of the problem.

- 1) The detection curve of conventional MD tells us that the Rayleigh resolution unit is rather a definition in the absence of noise since the detection rate of MD increases with SNR. Moreover, at  $\text{SNR} = 0/0$  dB, even at distances larger than the resolution unit, e.g.,  $\alpha = 1.2$ , the detection rate is still unsatisfactory.
- 2) The NLS, as a parametric spectral analysis method, is identical to an MLE under Gaussian noise with large  $N$  and high SNR. Hence, it should result in the highest detection rate if there is no prior knowledge about the true hypothesis. In Fig. 8, NLS gives a significantly improved probability of detection compared to MD. It is trivial, but important, to observe that the detection rate depends strongly on  $N \cdot \text{SNR}$ .
- 3) The SR power of SL1MMER is slightly better than NLS. The reason for the “better” performance of SL1MMER is that the  $L_1$  minimization gives us, for example, two possible positions of scatterers. The following model selection only decides between taking 0, 1, or 2 of those. NLS, on the other hand, estimates a new position for the one-scatterer case (probably located between the positions of the two-scatterer case). This renders the likelihood a little bit higher in NLS and makes NLS accept the one-scatterer case a little bit more often.

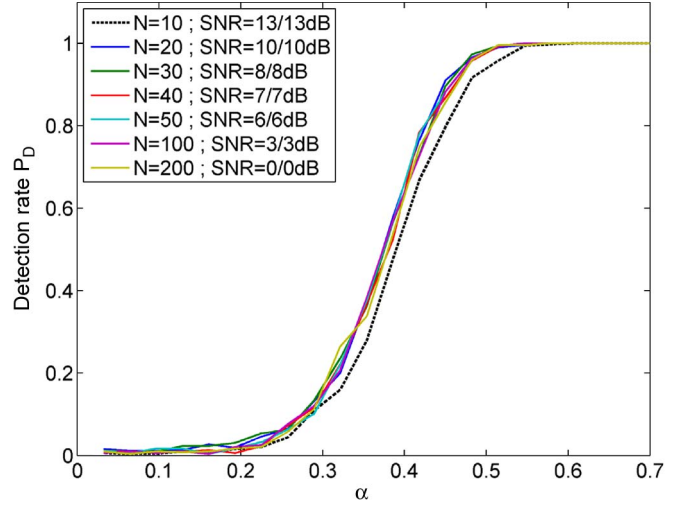


Fig. 9. Detection rate as a function of  $\alpha$  with fixed  $N \cdot \text{SNR}$  (aperture is regularly sampled) and  $\Delta\varphi = 0$ .

Due to the similarity between NLS and SL1MMER, all of the following results are approximately applicable to NLS as well, which is asymptotically optimal (see Fig. 7), and hence, they establish the absolute limit for SR.

### B. Dependence on $N \cdot \text{SNR}$

We expect the SR power of SL1MMER to depend asymptotically on the product  $N \cdot \text{SNR}$ , i.e., the number of acquisitions can be traded off against SNR. Fig. 9 shows the detection rates for different  $N$  versus SNR combinations for  $N \cdot \text{SNR}$  fixed to 400. As expected, the detection rate curves are consistent with each other in most cases. Only when  $N$  is very small, e.g.,  $N = 10$ , will the detection rate decrease slightly. In Section VII, we will show that the limit for  $N \cdot \text{SNR}$  to be invariant is at  $N \approx 15$ . Of course, besides  $N \cdot \text{SNR}$ , the detection rate would also depend on the phase difference of the two scatterers  $\Delta\varphi$ , which is assumed to be zero here.

### C. Dependence on Irregular Sampling

To give an impression about the impact of irregular sampling on detection rate, Fig. 10 shows an example of several simulations with  $N = 50$  uniformly distributed randomly sampled acquisitions at  $\text{SNR} = 6/6$  dB. The solid circle curve is the detection rate with regular samples, and it can be regarded as a reference. The solid square curve shows the same result using the particular irregularly distributed sample positions of the real data stack used in [15]. The solid black curve corresponds to irregular sampling, where the sampling distribution is uniform. From this plot, we get two important messages: first, the curves do not differ much from each other, and hence, irregular sampling does not have a large impact on SR (we have tried other sampling distributions, and they show very little effect.). Second, irregular sampling does not act as an additional difficulty; on the contrary, it can give a slightly better detection rate compared to regular sampling. Based on these observations, without loss of generality, we will use regular sampling in the range  $[-\Delta b, \Delta b]/2$  for the following examples.

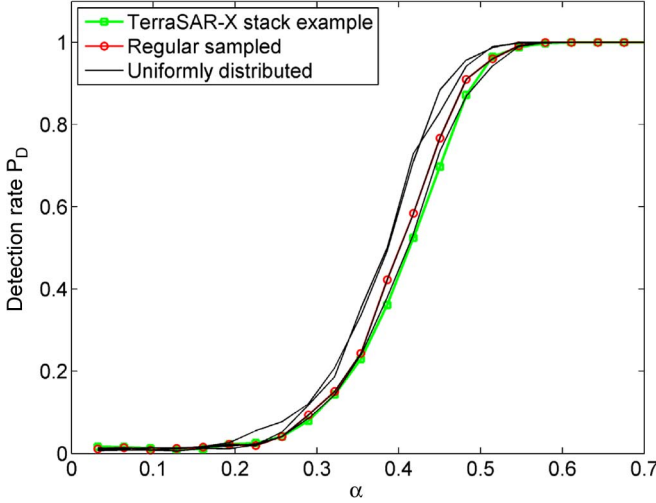


Fig. 10. Detection rate as a function of  $\alpha$  at  $N = 50$ ,  $\text{SNR} = 6/6$  dB, and  $\Delta\varphi = 0$  with regular sampling, uniformly distributed random sampling, and particular real-world aperture sample distribution from a TS-X data stack.

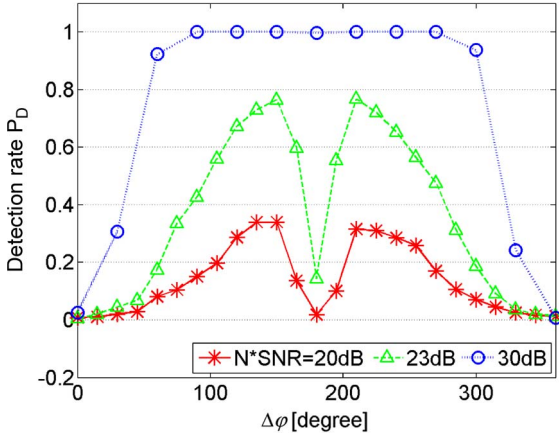


Fig. 11. Detection rate for  $\alpha = 0.15$  as a function of  $\Delta\varphi$  under different  $N \cdot \text{SNR}$ .

#### D. Dependence on Phase Difference

For  $\alpha < 1$ , the elevation estimation accuracy depends strongly on the phase difference  $\Delta\varphi$ , as shown in the last section. Fig. 11 shows an example of the detection rate as a function of  $\Delta\varphi$  under different  $N \cdot \text{SNR}$ , with  $\alpha = 0.15$ . It is not surprising that the detection rate varies dramatically with  $\Delta\varphi$ , and the worst case is  $\Delta\varphi = 0$ .

#### E. Fundamental Bound for SR

Followed by the aforementioned dependency analysis, in this section, we analyze the SR factor  $\kappa_{50\%} = \rho_s / \rho_{50\%}$ , which indicates the center point of the detection curve. Since the phase difference  $\Delta\varphi$  is a random variable and has a significant impact on detection rate, we average the detecting curves and then find the 50% point. The markers in Fig. 12 stand for  $\kappa_{50\%}$  from the simulations for varying  $N \cdot \text{SNR}$  within the range of interest (10–30 dB) under different amplitude ratios. It says that the achievable SR factors in this range

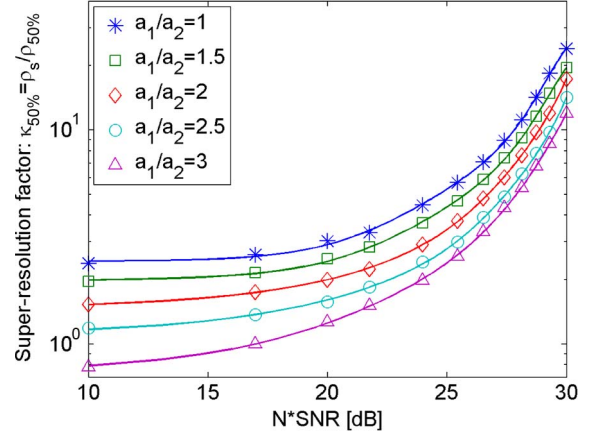


Fig. 12. SR factor averaged over  $\Delta\varphi$  as a function of  $N \cdot \text{SNR}$  under different amplitude ratios  $a_1/a_2$ . Experimental results (markers) versus polynomial fitting (solid lines).

typical for TomoSAR are promising and are on the order of 1.5–25. For the readers' convenience to further use our findings, we fit the experimental results to the following polynomial expansion:

$$\kappa_{50\%}(N \cdot \text{SNR}) = \sum_{i=0}^5 c_{SR,i}(N \cdot \text{SNR})^i \quad (27)$$

where  $c_{SR,i}$  is the coefficient for the  $i$ th order term of  $N \cdot \text{SNR}$ . Table I summarizes the coefficients for different amplitude ratios  $a_1/a_2$ , and the solid lines in Fig. 12 present the results of polynomial fitting. Although it is derived experimentally, the results in this section can be considered as the general fundamental bounds for SR of the imaging system.

## VII. MINIMUM NUMBER OF ACQUISITIONS

The previously shown examples demonstrate that the performance of tomographic reconstruction deviates from the  $N \cdot \text{SNR}$  dependence for small  $N$ . However, the required minimal number of acquisitions for robust reconstruction at a given SNR is of great interest since each SAR acquisition is expensive. In [29], the minimal number of tracks for the subspace methods for TomoSAR is proposed by assuming a sufficient SNR, which is rarely true for the spaceborne case. In this section, the robustness of the algorithm is defined by the minimal required number of acquisitions  $N_{\min,90\%}$  at a given SNR, which still allows detecting two scatterers with a distance of one Rayleigh resolution unit with  $\Delta\varphi = 0$  (the worst case) at a high probability ( $P_D \geq 90\%$ ). At a given SNR, we will provide an explicit expression for  $N_{\min,90\%}$ .

In the preceding section, we have seen that the detection rate has the same dependent factors as the CRLB. There is a correction  $1/N$  term in  $c_0$  to compensate the small  $N$  case. Introducing the same compensation factor which is  $N$  dependent as in (24), inserting  $\alpha = 1$ , and making some trivial normalization, we find that a 90% detection rate of two scatterers with a distance of  $\rho_s(\alpha = 1)$  can be achieved when the condition

TABLE I

POLYNOMIAL APPROXIMATION OF THE SR FACTOR AS A FUNCTION OF  $N \cdot \text{SNR}$ . COEFFICIENTS FOR DIFFERENT AMPLITUDE RATIOS  $a_1/a_2$ 

	$c_{SR,0}$	$c_{SR,1}$	$c_{SR,2} (\times 10^{-4})$	$c_{SR,3} (\times 10^{-6})$	$c_{SR,4} (\times 10^{-9})$	$c_{SR,5} (\times 10^{-12})$
$a_1/a_2=1$	2.4392	-0.0007	0.7116	-0.2013	0.2671	-0.1148
$a_1/a_2=1.5$	1.9717	0.0013	0.4374	-0.1197	0.1616	-0.0694
$a_1/a_2=2$	1.4691	0.0056	-0.0687	0.0392	-0.0444	0.0223
$a_1/a_2=2.5$	1.1108	0.0057	-0.1137	0.0463	-0.0531	0.0256
$a_1/a_2=3$	0.7343	0.0055	-0.0496	0.0147	-0.0064	0.0023

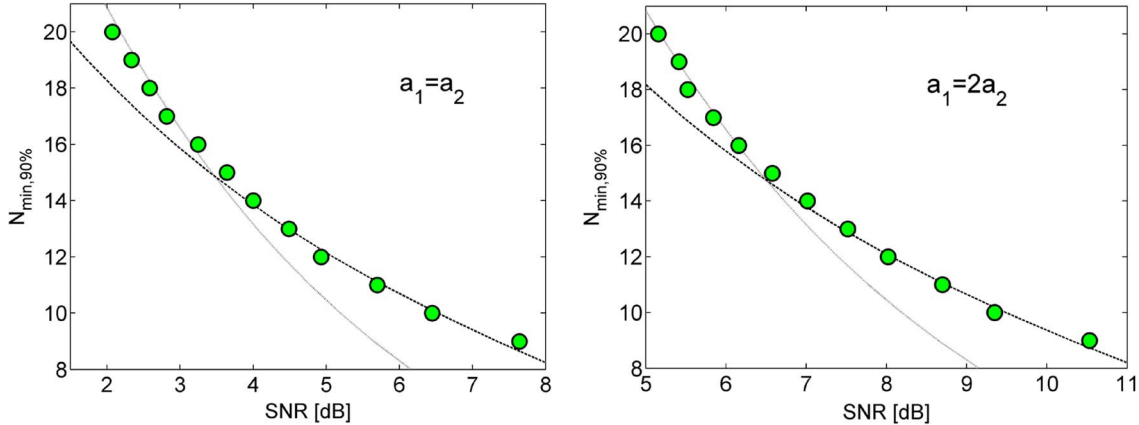


Fig. 13. Required minimal number of acquisitions  $N_{\min,90\%}$  for robust reconstruction (i.e., well detecting two scatterers ( $P_D \geq 90\%$ ) with a distance of one Rayleigh resolution unit) at a given SNR. Theory [dashed ( $N < 15$ ) and solid lines ( $N \geq 15$ )] versus experiment (circles). (Left)  $a_1 = a_2$ . (Right)  $a_1 = 2a_2$ . The worst case  $\Delta\varphi = 0$  is assumed.

shown in (28) holds (see equation at the bottom of the page).  $c_1$  and  $c_2$  are constants which depend on the amplitude ratio and phase difference between two scatterers.

In Fig. 13, the required minimal number of acquisitions  $N_{\min,90}$  for different amplitude ratios [ $a_1 = a_2$  (left) and  $a_1 = 2a_2$  (right)] and for  $\Delta\varphi = 0$  is presented. The circles show the 90% detection rate positions with  $N \in [8, 20]$ . For example, for a total SNR of 6 dB, only 11 acquisitions are required for  $a_1 = a_2$  (SNR = 3/3 dB, respectively), while 17 acquisitions are needed for  $a_1 = 2a_2$  (SNR = 5/1 dB, respectively). From the aforementioned experimental results, according to (28), we get  $c_1 = 54.2$  and  $c_2 = 33.1$  for  $a_1 = a_2$  and  $\Delta\varphi = 0$ , and  $c_1 = 107.3$  and  $c_2 = 65.9$  for  $a_1 = 2a_2$  and  $\Delta\varphi = 0$ . The dashed ( $N < 15$ ) and solid lines ( $N \geq 15$ ) in Fig. 13 show the estimated  $N_{\min,90\%}$  from (28) with the aforementioned estimated  $c_1$  and  $c_2$ . For  $N \geq 15$ ,  $N$  and SNR can be traded for  $N \cdot \text{SNR} = \text{const.}$

### VIII. CONCLUSION AND FINAL STATEMENTS

In this paper, we have investigated the elevation estimation accuracy, SR power, and robustness of sparse signal reconstruction from random and regular spectral samples for the application of TomoSAR. The results are obtained by the CS-

based algorithm SLIMMER and are compared to NLS. They thus establish absolute bounds for SR. In particular, with (25) and (27), we have provided easy-to-use analytical expressions for location accuracy and SR factors.

A few additional remarks might be helpful for further use of our results.

- 1) The minimal separable distance between two interfering scatterers depends significantly on the phase difference  $\Delta\varphi$ , which is random. Hence, we investigated the SR power in a more general way, i.e., assuming that  $\Delta\varphi$  is uniformly distributed in  $[-\pi, \pi]$  instead of given a specific value. The theoretically achievable SR factors in the low- $N$  and low-SNR situations of TomoSAR are promising and are on the order of 1.5–25.
- 2) We have shown that regular and irregular aperture sample distributions yield approximately the same results. This is only true for the SR problem, i.e., when two scatterers are close. The irregular distribution, though, has an additional advantage when it comes to imaging of reflectivity profiles of large support in elevation  $s$ . Compared to regular aperture sampling, it does not suffer from strong and discrete ambiguities.

$$\begin{cases} N_{\min,90\%} \cdot \text{SNR} \cdot \left( 2.5 - 1.5 \cos \left( 2\Delta\varphi + 2\pi \left( 1 - \frac{1}{N_{\min,90\%}} \right) \right) \right)^2 = c_1, & N_{\min,90\%} < 15 \\ N_{\min,90\%} \cdot \text{SNR} = c_2, & N_{\min,90\%} \geq 15 \end{cases} \quad (28)$$

- 3) If the sample distribution is not rectangular with width  $\Delta b$  but, for example, Gaussian, then similar results apply as if a rectangular distribution with the same standard deviation  $\sigma_b$  was used. In our equations, only  $\Delta b$  has to be replaced with  $\sqrt{12}\sigma_b$ .
- 4) We have restricted ourselves to 1-D spectral estimation. Although the results are easily extendable to the 2-D case, i.e., motion retrieval by D-TomoSAR, there are a few subtleties to be considered. For example, a possible correlation between the temporal and spatial coordinates of the 2-D aperture sampling pattern has some influence on the 2-D SR power. This will be addressed in a further study.
- 5) Sparsity is the prerequisite of CS-based algorithms such as SL1MMER. This property is always ensured for point-like scatterers, independent of the SAR system's range or elevation resolutions. Rough surfaces, assumed to be mostly either horizontal or vertical, require  $\rho_r \ll \min\{\rho_s \tan \theta, \rho_s / \sin \theta\}$  for appearing sparse in elevation, where  $\theta$  is the incidence angle. The experimental results [13], [30], however, have shown that the CS-based estimators degrade gracefully with the loss of sparsity. Even in the case of ERS with an almost isotropic resolution cell, a moderate improvement over linear estimators can be achieved.

#### ACKNOWLEDGMENT

The authors would like to thank R. Brcic from DLR for the valuable discussions.

#### REFERENCES

- [1] F. Lombardini, "Differential tomography: A new framework for SAR interferometry," in *Proc. IGARSS*, Toulouse, France, 2003, pp. 1206–1208.
- [2] G. Fornaro, D. Reale, and F. Serafino, "Four-dimensional SAR imaging for height estimation and monitoring of single and double scatterers," *IEEE Trans. Geosci. Remote Sens.*, vol. 47, no. 1, pp. 224–237, Jan. 2009.
- [3] X. Zhu and R. Bamler, "Very high resolution spaceborne SAR tomography in urban environment," *IEEE Trans. Geosci. Remote Sens.*, vol. 48, no. 12, pp. 4296–4308, Dec. 2010.
- [4] R. Bamler, M. Eineder, N. Adam, X. Zhu, and S. Gernhardt, "Interferometric potential of high resolution spaceborne SAR," *Photogramm. Fernerkundung Geoinformation*, vol. 5, pp. 407–419, Nov. 2009.
- [5] N. Adam, M. Eineder, N. Yague-Martinez, and R. Bamler, "High-resolution interferometric stacking with TerraSAR-X," in *Proc. IGARSS*, Boston, MA, 2008, pp. II-117–II-120.
- [6] X. Zhu and R. Bamler, "Let's do the time warp: Multi-component nonlinear motion estimation in differential SAR tomography," *IEEE Geosci. Remote Sens. Lett.*, vol. 8, no. 4, pp. 735–739, Jul. 2011.
- [7] E. Candès, "Compressive sampling," in *Proc. Int. Congr. Math.*, Madrid, Spain, 2006, vol. 3, pp. 1433–1452.
- [8] R. Baraniuk, "Compressive sensing," *IEEE Signal Process. Mag.*, vol. 24, no. 4, pp. 118–121, Jul. 2007.
- [9] D. Donoho, "Compressed sensing," *IEEE Trans. Inf. Theory*, vol. 52, no. 4, pp. 1289–1306, Apr. 2006.
- [10] J. H. G. Ender, "On compressive sensing applied to radar," *Signal Process.*, vol. 90, *Special Section on Statistical Signal & Array Processing*, no. 5, pp. 1402–1414, May 2010.
- [11] L. Zhang, M. Xing, C. Qiu, J. Li, and Z. Bao, "Achieving higher resolution ISAR imaging with limited pulses via compressed sampling," *IEEE Geosci. Remote Sens. Lett.*, vol. 6, no. 3, pp. 567–571, Jul. 2009.
- [12] M. Tello Alonso, P. López-Dekker, and J. J. Mallorquí, "A novel strategy for radar imaging based on compressive sensing," *IEEE Trans. Geosci. Remote Sens.*, vol. 48, no. 12, pp. 4285–4295, Dec. 2011.
- [13] A. Budillon, A. Evangelista, and G. Schirinzi, "Three dimensional SAR focusing from multi-pass signals using compressive sampling," *IEEE Trans. Geosci. Remote Sens.*, vol. 49, no. 1, pp. 488–499, Jan. 2011.
- [14] A. Budillon, A. Evangelista, and G. Schirinzi, "SAR tomography from sparse samples," in *Proc. IEEE IGARSS*, Cape Town, South Africa, 2009, pp. IV-865–IV-868.
- [15] X. Zhu and R. Bamler, "Tomographic SAR inversion by L1 norm regularization—The compressive sensing approach," *IEEE Trans. Geosci. Remote Sens.*, vol. 48, no. 10, pp. 3839–3846, Oct. 2010.
- [16] G. Fornaro, F. Serafino, and F. Lombardini, "Three-dimensional multi-pass SAR focusing: Experiments with long-term spaceborne data," *IEEE Trans. Geosci. Remote Sens.*, vol. 43, no. 4, pp. 702–714, Apr. 2005.
- [17] X. Zhu, "High-Resolution Spaceborne Radar Tomography," M.S. thesis, Lehrstuhl für Methodik der Fernerkundung, Technische Universität München, Munich, Germany, 2008, Lehrstuhlbibliothek.
- [18] J. Rissanen, A Short Introduction to Model Selection, Kolmogorov Complexity and Minimum Description Length, 2005. [Online]. Available: [www.mdl-research.org](http://www.mdl-research.org)
- [19] K. P. Burnham and D. R. Anderson, "Multimodel inference: Understanding AIC and BIC in model selection," *Sociol. Methods Res.*, vol. 33, no. 2, pp. 261–304, 2004.
- [20] G. Schwarz, "Estimating the dimension of a model," *Ann. Statist.*, vol. 6, no. 2, pp. 461–464, Mar. 1978.
- [21] J. Rissanen, "Modelling by shortest data description," *Automatica*, vol. 14, no. 5, pp. 465–471, Sep. 1978.
- [22] P. Stoica and R. Moses, *Spectral Analysis of Signals*. Englewood Cliffs, NJ: Prentice-Hall, 2005.
- [23] D. N. Swigler, "Frequency estimation for closely spaced sinusoids: Simple approximations to the Cramér–Rao lower bound," *IEEE Trans. Signal Process.*, vol. 41, no. 1, p. 489, Jan. 1993.
- [24] S. Tebaldini and A. M. Guarnieri, "On the role of phase stability in SAR multibaseline applications," *IEEE Trans. Geosci. Remote Sens.*, vol. 48, no. 7, pp. 2953–2966, Jul. 2010.
- [25] M. Shahram and P. Milanfar, "Improved spectral analysis of nearby tones using local detectors," in *Proc. Int. Conf. Acoust., Speech, Signal Process.*, Philadelphia, PA, Mar. 2005, pp. iv/637–iv/640.
- [26] A. M. Bruckstein, D. L. Donoho, and M. Elad, "From sparse solutions of systems of equations to sparse modeling of signals," *SIAM Rev.*, vol. 51, no. 1, pp. 34–81, 2009.
- [27] S. S. Chen, D. L. Donoho, and M. A. Saunders, "Atomic decomposition by basis pursuit," *SIAM Rev.*, vol. 43, no. 1, pp. 129–159, 2001.
- [28] D. Wilkes and J. Cadzow, "The effects of phase on high-resolution frequency estimators," *IEEE Trans. Signal Process.*, vol. 41, no. 3, pp. 1319–1330, Mar. 1993.
- [29] M. Nannini, R. Scheiber, and A. Moreira, "Estimation of the minimum number of tracks for SAR tomography," *IEEE Trans. Geosci. Remote Sens.*, vol. 47, no. 2, pp. 531–543, Feb. 2009.
- [30] X. Zhu and G. Fornaro, 2009, Unpublished results with ERS data stacks over the city of Roma.



**Xiao Xiang Zhu** (S'10) received the B.S. degree in space engineering from the National University of Defense Technology, Changsha, China, in 2006 and the M.Sc. and Dr.-Ing. degrees from Technische Universität München (TUM), Munich, Germany, in 2008 and 2011, respectively.

In October/November 2009, she was a Guest Scientist at the Italian National Research Council (CNR)—Institute for Electromagnetic Sensing of the Environment (IREA), Naples, Italy. Since May 2011, she has been a full-time Scientific Collaborator with the Remote Sensing Technology Institute, German Aerospace Center (DLR), Wessling, Germany, and with the Remote Sensing Technology Department, TUM. Her main research interests are signal processing, including innovative algorithms such as compressive sensing and sparse reconstruction, with applications in the field of remote sensing, particularly 3-D, 4-D, or higher dimensional SAR imaging.

Her Ph.D. dissertation "Very High Resolution Tomographic SAR Inversion for Urban Infrastructure Monitoring—A Sparse and Nonlinear Tour" won the Dimitri N. Chorafas Foundation Research Award in 2011 for its distinguished innovativeness and sustainability.



**Richard Bamler** (M'95–SM'00–F'05) received the Diploma degree in electrical engineering, the Doctorate degree in engineering, and the "Habilitation" in the field of signal and systems theory from Technische Universität München (TUM), Munich, Germany, in 1980, 1986, and 1988, respectively.

He worked at the university from 1981 to 1989 on optical signal processing, holography, wave propagation, and tomography. He joined the German Aerospace Center (DLR), Oberpfaffenhofen, Germany, in 1989, where he is currently the Director of the Remote Sensing Technology Institute. In early 1994, he was a Visiting Scientist at the Jet Propulsion Laboratory (JPL) in preparation of the SIR-C/X-SAR missions, and in 1996, he was a Guest Professor with the University of Innsbruck, Innsbruck, Austria. Since 2003, he has been a full Professor in remote sensing technology with the TUM as a double appointment with his DLR position. His teaching activities include university lectures and courses on signal processing, estimation theory, and SAR. Since 2010, he has been a member of the executive board of Munich Aerospace, which is a newly founded research and education project between Munich universities and extramural research institutions, including DLR. Since he joined DLR, he, his team, and his institute have been working on SAR and optical remote sensing, image analysis and understanding, stereo reconstruction, computer vision, ocean color, passive and active atmospheric sounding, and laboratory spectrometry. They were and are responsible for the development of the operational processors for SIR-C/X-SAR, SRTM, TerraSAR-X, TanDEM-X, ERS-2/GOME, Envisat/SCIAMACHY, MetOp/GOME-2, and EnMAP. He is the author of more than 200 scientific publications, among them about 50 journal papers and a book on multidimensional linear systems theory. He is the holder of eight patents and patent applications in remote sensing. His current research interests are in algorithms for optimum information extraction from remote sensing data, with emphasis on SAR. This involves new estimation algorithms, like sparse reconstruction and compressive sensing. He has devised several high-precision algorithms for monostatic and bistatic SAR processing, SAR calibration and product validation, GMTI for traffic monitoring, SAR interferometry, phase unwrapping, persistent scatterer interferometry, and differential SAR tomography.